applied sciences

MDPI

Article

Numerical Research on the Effects of Process Parameters on Microdroplet Jetting Characteristics by Piezoelectric Printhead

Hong Liu [1,*], Ting Lei [1], Xiaohui Nan [1] and Fan Peng [2]

[1] College of Mechatronic Engineering, North Minzu University, Yinchuan 750021, China
[2] Kocel Machinery Limited, Yinchuan 750021, China
* Correspondence: hlongiu@163.com; Tel.: +86-18161511196

Abstract: The precision and consistency of the microdroplet jetting procedure are crucial for the casting sand mold's performance during binder injection. The generation and jetting of microdroplets in piezoelectric printheads were examined in this study in relation to changes in specific jetting process parameters. Using finite element analysis and a simplified physical model of a microdroplet jetting device, an electromechanically coupled model of a microdroplet jetting device was created in order to study the characteristics of microdroplet jetting. A volume-of-fluid model was also created in order to study the microdroplet jetting process and perform repeatability tests. The effects of altering nozzle radius, actuation pulse width, intake velocity, and fluid viscosity on microdroplet jetting properties were then investigated using the models. We were able to control the development of satellite droplets thanks to the knowledge we gained about how each process parameter affected droplet status. This study demonstrates how the radius of the nozzle and the pulse width of the piezoelectric actuation signal have a significant impact on the jetting properties of piezoelectric printheads and the production of microdroplets. The quantitative correlations between process factors and jetting characteristics can be used to optimize microdroplet production and reduce droplet size. Finally, this study will help create control systems for microdroplet jetting operations and enhance the precision of 3D printed casting sand molds.

Keywords: 3D printing; casting sand mold; piezoelectric printheads; microdroplet injection; forming accuracy

Citation: Liu, H.; Lei, T.; Nan, X.; Peng, F. Numerical Research on the Effects of Process Parameters on Microdroplet Jetting Characteristics by Piezoelectric Printhead. *Appl. Sci.* **2023**, *13*, 4452. https://doi.org/10.3390/app13074452

Academic Editor: César M. A. Vasques

Received: 11 February 2023
Revised: 25 March 2023
Accepted: 29 March 2023
Published: 31 March 2023

1. Introduction

Additive manufacturing is crucial to the national development strategy of China. The large-scale development and utilization of inkjet 3D printing for sand mold production are important for the transformation and sustainable development of the foundry industry in China. Significant study topics include inkjet printing's techniques, equipment, forming quality, and quality control. In particular, high-precision sand casting molds should be produced using 3D printing technology in order to eliminate secondary processing [1].

The forming precision of printed sand molds can be improved by improving the structural design of the printhead [2], increasing the number of arrayed printheads [3], and enabling the inter-nozzle spacing to be mechanically altered [4]. However, improving the forming precision by these means inevitably leads to two new problems: first, multiplying the number of printheads to create arrayed printheads greatly increases the overall cost of the 3D printing system. The consequent increase in weight also decreases mechanical precision. Second, increasing the liquid-to-solid ratio of the feed fluid causes the mechanical strength of the sand mold to greatly exceed standard strength values, which makes it difficult to remove the sand mold from complex casted cavities and causes surface defects, such as pores and sand inclusions [5]. These issues significantly curtail the strengths of the 3D inkjet printing technique. Recently, it has been shown that forming precision can be improved significantly by tuning the volumetric dimensions and jetting velocities of

the jetted microdroplets according to the specific requirements of the task at hand [6,7]. Therefore, some scholars have concluded that the tuning of microdroplet jetting characteristics to solve the sand mold printing problems is essential for the overall optimization and operation of 3D sand printing systems [8–10]. To optimize process parameters, the effects of jetting frequency, standoff distance (distance between the nozzle and printing substrate), and printing speed on inkjet printing precision were studied [11]. Presently, there is a substantial body of research on the relationship between printing parameters and printing quality. Miyanaji et al. [12] from the University of Louisville experimentally studied the effects of printing speed on printing quality and found that increasing printing speed always decreases precision owing to the intensification of inertial effects, regardless of standoff distance. Lei et al. [13] studied spray-printed straight lines to construct a model that predicts the effects of printing speed on forming dimensions, and they performed simulations to validate the ability of their model to predict the dimensions of 3D printed products accurately. Although jetting frequency is an important process parameter that affects forming efficiency, it is inversely related to printing speed. Printing resolution is maximized when jetting frequency is increased and printing speed is reduced, and vice versa; forming precision is also affected by jetting frequency [14]. Coniglio et al. [15] studied the effects of process parameters on the quality and anisotropic properties of 3D printed casting sand molds and used an experimentally validated mathematical model to show that printing quality is strongly dependent on the selection of process parameters. The aforementioned studies show that the effects of each process parameter on printing quality are well established, which is critical for the development of optimal process routes. However, a profound understanding of the basic characteristics of microdroplet jetting and the combined effects of all process parameters is necessary to homogenize and stabilize inkjet performance. Because microdroplet characteristics are affected by many parameters, determining the relationship between jetting and forming and their effects on the quality of printed sand molds are crucial. The Goto group performed quantitative analyses on the effects of binder content on 3D sand mold printing and found that current sand mold printing processes often use excessively high binder concentrations, which is detrimental to printing quality [16]. Sama et al. [17] studied inkjet processes from a fluid flow perspective and listed the factors that can affect the jetting performance of a printhead. They also noted that microdroplets are often accompanied by a large number of satellite droplets, which is a significant factor contributing to microdroplet landing errors. The Liu ZP group [18] designed and fabricated a piezoelectric printhead and used a laser displacement measurement system to measure its microdroplet characteristics (such as microdroplet volume). They analyzed the factors affecting these characteristics based on actuation structure and found strategies to minimize the occurrence of satellite droplets. The findings of a previous study also indicate that the appearance of uncontrolled satellite droplets around the main droplets affects the quality and performance of 3D printed products [19–21]. Wang et al. [22] succeeded in eliminating all satellite droplets during 3D sand mold printing by manually destabilizing the feed pressure. However, this significantly increased the amount of fluid required to manufacture the mold and substantially reduced the final dimensions of the sand mold. This study also indirectly showed that excess microdroplet jetting affects dimensional accuracy adversely. Although these results show that excess microdroplet jetting volumes and satellite droplets affect dimensional accuracy significantly, the relationship between microdroplet volume and printing precision was not quantified. The aforementioned studies also show that the use of simulation and experimental approaches to improve inkjet control strategies based on microdroplet jetting characteristics and behaviors is crucial for improving inkjet printing quality. However, in the context of sand mold printing (particularly for high-precision sand molds), studies on microdroplet jetting behaviors and their effects on sand mold printing quality remain scarce.

Therefore, this work aims to study microdroplet formation and deposition in the presence of electromechanical coupling by simulating the jetting processes of a piezoelectric printhead with varying control inputs, internal structures, and inkjet fluid properties. The

relationship between structural and process parameters and microdroplet jetting behaviors was studied, and tuning strategies were formulated to improve jetting quality. The findings of this work can assist future efforts to enhance the printing quality of high-precision printed sand molds.

2. Principle of Microdroplet Jetting

2.1. Principles of Droplet Jetting

Figure 1 depicts the operational principles of a piezoelectric printer. The piezoelectric printhead consists of a composite piezoelectric diaphragm (piezoelectric actuator), fluid and gas intake, sealing rings, liquid working chamber, and droplet nozzle. In the presence of a pulse signal, the piezoelectric ceramic experiences the inverse piezoelectric effect, causing the ceramic to expand or contract (bend). When a negative voltage is given, the piezoelectric diaphragm attached to one of the chamber's walls compresses and sucks fluid into the chamber. In contrast, the application of a positive voltage causes the diaphragm to expand, decreasing the working chamber's capacity and generating a pressure fluctuation that forces the fluid out of the nozzle. The fluid then undergoes column stretching, neck shrinking, and breaking to produce a droplet, which subsequently flies through the air and deposits itself on the substrate.

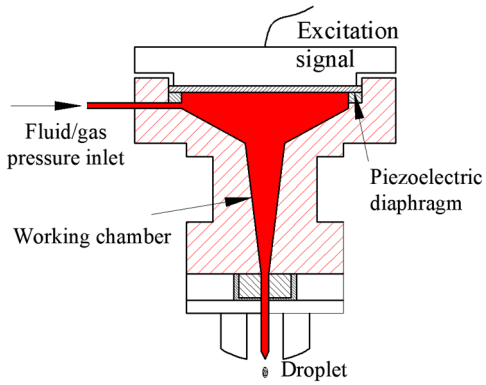

Figure 1. Operating principles of a piezoelectric printhead.

2.2. Microdroplet Formation Criterion

Microdroplets are formed at the mouth of the nozzle due to the periodic vibrations of the piezoelectric actuator [23]. To form a microdroplet, the volume of the droplet formed by this process must exceed a standard droplet volume and satisfy Equations (1) and (2) [24]:

$$W_e = \frac{\rho v_0(t) r_0}{\sigma} > 4, \tag{1}$$

$$V = \pi {r_0}^2 \int_0^{t_1} v_0(t) dt \geq \frac{4\pi {r_0}^3}{3} \tag{2}$$

where W_e is the ratio of the inertia of the fluid to its surface tension, ρ is the density of the droplet fluid/material, σ is the surface tension coefficient of the droplet fluid/material, $v_0(t)$ is the axial velocity of the fluid, and r_0 is the radius of the nozzle channel.

3. Construction of an Electromechanically Coupled Model to Describe Microdroplet Formation and Jetting

It is speculated that microdroplet production and jetting include electromechanical coupling through piezoelectric actuation and complex fluid changes inside the working chamber. In this part, a mechanical model of microdroplet production and jet creation inside a structural displacement field was built using the principles of conservation of mass and momentum. Integration was then used to determine the link between the structural displacement field and the electric field. Finally, an electromechanically connected model of

microdroplet production and jetting was constructed by substituting electric field terms for displacement field terms in the mechanical model. Figure 2 depicts a simplified diagram of droplet production and jet development that illustrates the electromechanical connections of the model. The model comprises a fluid supply system, a fluid line connecting the supply to the nozzle, a fluid chamber, a nozzle, and a piezoelectric actuator.

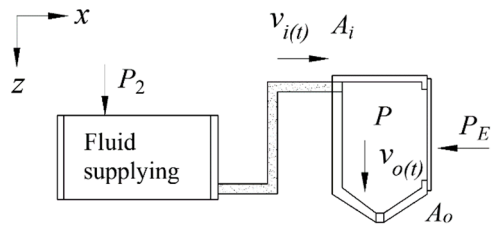

Figure 2. Simplified physical model of microdroplet jetting.

Considering that a metallic diaphragm with surface area A vibrates at a rate of dz/dt and the inlet flow rate is $v_i(t)$, the nozzle flow rate is $v_0(t)$, the inlet area is A_i, and the nozzle area is A_0, we obtain the following equations using the law of mass conservation:

$$\frac{d}{dt}(\rho V) + \rho v_0 A_0 + \rho v_i A_i = 0, \tag{3}$$

$$\frac{d}{dt}(\rho V) = V\frac{d\rho}{dt} + \rho\frac{dV}{dt}, \tag{4}$$

$$\frac{dV}{dt} = -K_v A\frac{d}{dt}, \tag{5}$$

$$\frac{d\rho}{dt} = \rho K_s\frac{dP}{dt}, \tag{6}$$

where ρ is the fluid density, and K_v is the velocity variation coefficient of the fluid inside the working chamber.

When an electrical signal is applied, the piezoelectric actuator generates a displacement perpendicular to the diaphragm. The mathematical description of piezoelectricity is provided by the following equations:

$$S_1 = s_{11}^E T_1 + d_{31} E_3, \tag{7}$$

$$D_3 = d_{31} T_1 + \epsilon_{33}^T E_3, \tag{8}$$

where S_1 and T_1 are the strain and stress in the x-direction, respectively; E_3 and D_3 are the electric field and the electric flux density in the z-direction, respectively; ϵ_{33}^T is the dielectric constant when the external stress is equal to zero or a constant; d_{31} is the piezoelectric constant; and s_{11}^E is the elastic compliance coefficient when the electric field is equal to zero or a constant.

If the electric field of the piezoelectric actuator is assumed to be homogeneous, then E_3 is a linear function of the voltage U applied between the ends of the piezoelectric ceramic. If the maximum displacement of the piezoelectric actuator in the vertical direction is z, the force–displacement equation of the piezoelectric actuator is as follows:

$$z = \alpha U - \beta F, \tag{9}$$

where α and β are constants, z is the maximum displacement, U is the driving voltage, and F is the external force applied to the piezoelectric ceramic chip. The equation specifies the relationship between the physical quantities z, U, and F.

The model that equates the electric and displacement fields of the piezoelectric actuator can be simplified into an elastic system with a diaphragm of mass m and elastic modulus k (Figure 3). The force equation of this system may be expressed as

$$m\frac{d^2z}{dt^2} + \left(k + \frac{1}{\beta}\right)z = \frac{\alpha}{\beta}\phi - PA, \tag{10}$$

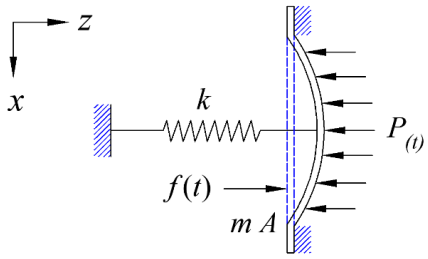

Figure 3. Forces of a piezoelectric actuator.

Based on the mechanical displacement field model and the equivalence of displacement and electric fields, Equation (10) may be rewritten as

$$\frac{dP}{dt} = \frac{1}{k_s V}\left(K_v A\frac{dz}{dt} - v_0 A_0 - v_i A_i\right), \tag{11}$$

This equation describes microdroplet generation. According to the conservation of energy and the unsteady Navier–Stokes equation, the movements of the microdroplet during jetting may be described by

$$\int_1^2 \frac{\partial v}{\partial t}ds + \left(\frac{P}{\rho} + \frac{1}{2}v^2 + gz\right)_2 - \left(\frac{P}{\rho} + \frac{1}{2}v^2 + gz\right)_1 = 0, \tag{12}$$

where s, P, and v are the displacement, pressure, and velocity of the fluid, respectively, and g is the gravitational acceleration.

In order to create a model that describes the relationship between actuation parameters, structural parameters, and microdroplet movements, the periodic expansion and contraction of the piezoelectric actuator was accounted for, and Equations (11) and (12) were utilized to describe microdroplet formation and jetting.

4. Determination of Simulation Parameters

4.1. Determining the Characteristics of the Composite Piezoelectric Diaphragm

At low voltages, the PZT-5 piezoelectric crystal exhibits enormous stresses that are linearly proportional to the strength of the applied electric field, making it ideally suited for printer applications. Therefore, the model's piezoelectric diaphragm parameters were configured based on the characteristics of the PZT-5 piezoelectric crystal. Since the droplet fluid was moderately corrosive, the diaphragm required an anticorrosion plating. Therefore, a corrosion-resistant and easily deformable (low elastic modulus) brass sheet was applied to the diaphragm. In the simulation model, the composite piezoelectric ceramic membrane consisted of a brass film and PZT-5 piezoelectric crystal.

4.2. Relationship between Structural Parameters and Droplet State

Microdroplet formation necessitates that the size of the piezoelectric actuator permits resonant operation while also giving a suitably large amplitude. The differential equation that explains vibrational displacements along the thickness of a diaphragm in a vacuum, according to vibration theory, is

$$\nabla^4\xi = -\frac{\rho\partial^2\xi}{W\partial t2} \tag{13}$$

Here, $W = \frac{Et^2}{121-v^2}$, $\xi = \frac{\rho_1 D}{\rho_2 t}$, and D is the effective diameter of the composite diaphragm. $\rho = \frac{m_e}{V_e}$ is its effective density, m_e is the total mass of the composite diaphragm, V_e is the effective volume of the composite diaphragm, and v is the Poisson's ratio of the material.

The resonant frequency is given by

$$f = 0.4534 \frac{t{\beta_{ab}}^2}{D^2} \sqrt{\frac{E}{\rho(1-v^2)}}. \tag{14}$$

According to the structural model shown in Figure 2, if pressure losses along the pressure inlet are negligible, the pressure of the liquid in the working chamber P when the piezoelectric actuator is vibrating can be expressed as

$$P = \frac{4K_T \Delta h}{K_y h}, \tag{15}$$

where Δh is the vibrational amplitude of the composite diaphragm, $K_y = \frac{4\Delta V}{\pi D^2 \Delta h}$ is the volume change coefficient of the liquid inside the working chamber, D is the internal diameter of the chamber, and h is the depth of the chamber.

As inlet pressure losses must be accounted for in practical applications [25], the relationship between the vibrational amplitude of the piezoelectric actuator and the dimensions of the membrane is given by

$$\Delta h = K_p \frac{UK_y}{r_0^2}. \tag{16}$$

Here, U is the amplitude of the exciting voltage. Once the voltage is known, the dimensions of the piezoelectric actuator can be determined accurately using the aforementioned equations.

4.3. Design of the Working Chamber

The interior diameter of the working chamber can be considered as the diameter of the composite piezoelectric diaphragm, and the nozzle diameter is typically determined based on the printing process's needs. The relevant dimensions of the working chamber are therefore the depth of the liquid within the chamber, the size of the fluid supply intake, and the aspect ratio of the nozzle. When the vibrations of the piezoelectric actuator generate pressure, the fluid in the working chamber simultaneously exits the fluid supply inlet and nozzle. Given a viscous fluid, the equation for the thickness of the boundary layer is:

$$\delta = \sqrt{\psi t_w}. \tag{17}$$

The pulse width t_w is given by

$$t_w = 1.633 \frac{\rho L r_0}{p} \approx \frac{V}{v_0 A} \tag{18}$$

The relationship between lost flow Q and the diameters of the fluid supply inlet and nozzle (r_1 and r_2) is then given by

$$Q = \frac{r_1}{r_1^2 + r_0^2} \tag{19}$$

5. Model for the Simulation of Microdroplet Jetting Processes

The impacts of external control inputs, feed characteristics, and structural dimensions on the jetting process were examined using finite element analysis and numerical simulations based on the previously discussed electromechanically coupled model and model-derived structural parameters.

The droplet transitions from the fluid domain to the air domain during microdroplet jetting. A piezoelectric intake, walls, a fluid collection zone, and a throttling channel make up the fluid domain. With its modest domain areas, the straightforward and centrally symmetrical model proved computationally efficient and fitted the needs of the investigation. For the modeling of jetting operations and turbulence analysis in the throttling channel, the simplified model shown in Figure 4 was utilized.

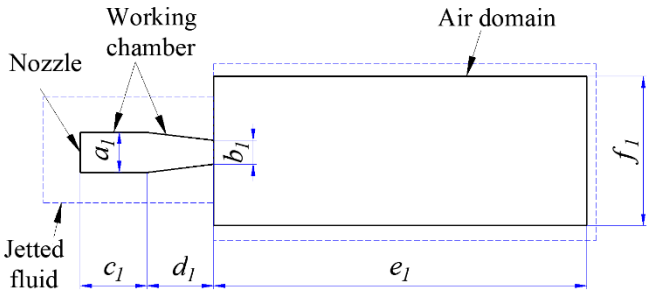

Figure 4. Simplified simulation model.

In Figure 4, all parameters are modeled according to the dimensions of the printhead of the selected model. b_1 is the nozzle diameter, a_1 is the diameter of the working chamber output to the nozzle, c_1 is the length of the chamber, d_1 is the nozzle length, and e_1 is the proposed air domain length (jetting distance).

When the piezoelectric actuator vibrates, the diaphragm converts the compression in the fluid domain chamber into a velocity, which varies sinusoidally with a velocity amplitude of V_{max}. Therefore, a user-defined function was used in ANSYS FLUENT to define velocity at the piezoelectric inlet based on V_{max}. The simulation parameters that correspond to a V_{max} of 2.200 m/s are shown in Table 1.

Table 1. Simulation parameters when V_{max} = 2.200 m/s.

Material	Density (kg/m^3)	Viscosity (cp)	Characteristic Length (mm)	Reynolds Number	Turbulence Intensity (%)	Surface Tension (dyn/m)
Furan resin	2100.00	9.00	0.03	15,750.00	0.04780	50

6. Simulation of Microdroplet Injection Process

6.1. Analysis of Microdroplet Formation

A simulation-based qualitative analysis of the jetting processes was performed using furan resin as the jetted fluid. Driving velocity, amplitude, nozzle diameter, and feed attributes were varied to investigate the effects of these parameters on microdroplet formation. In this experiment, the pulse width t_w was set to 10 µs, and V_{max} was set to 2.500 m/s. Several steps of the microdroplet formation process are demonstrated in Figure 5.

Figure 5 depicts the steps of microdroplet development: column elongation, neck contraction, column rupture to create the droplet, and steady movement. As shown, a satellite droplet split from the original droplet. This was caused by the working chamber's excess fluid leak, which was triggered by the composite diaphragm's movement. It is challenging to guarantee that the deformation of the composite diaphragm is exactly in line with the physicochemical parameters of the fluid during an actual printing process since numerous elements influence the motions of the fluid in the printhead. The satellite droplet, however, may be able to catch up with the primary droplet throughout its flight to the substrate because it has a lower volume and is consequently susceptible to less drag. Therefore, by either decreasing the satellite droplet's volume or increasing its flight speed, the satellite and main droplets can be combined. The correlation between the satellite and primary droplet flying speeds is seen in Figure 6.

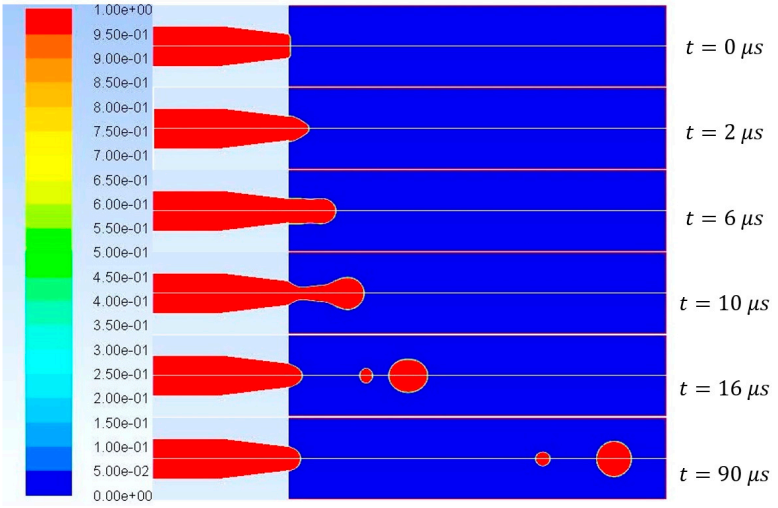

Figure 5. Microdroplet states during the jetting process.

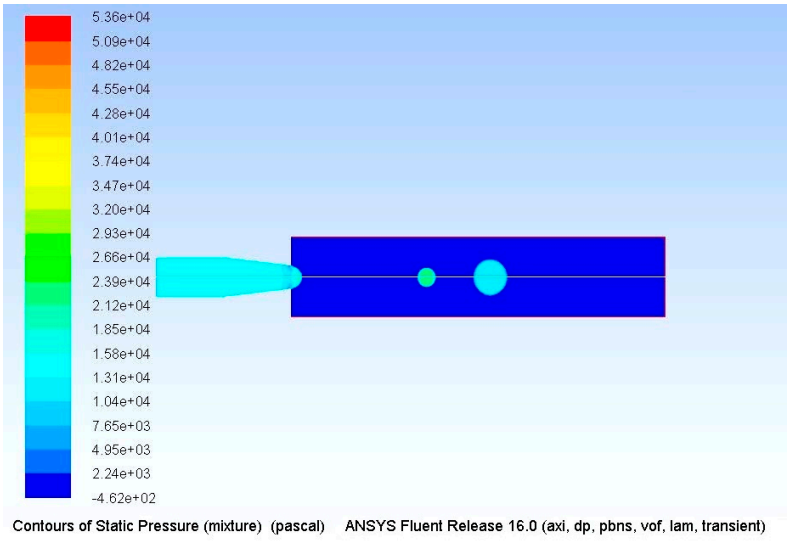

(**a**)

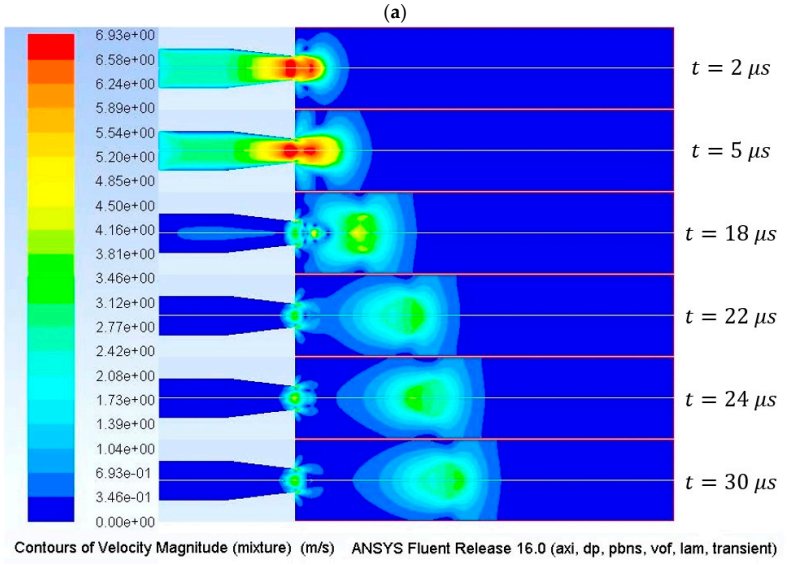

(**b**)

Figure 6. Physical behaviors of droplet jetting, (**a**) pressure contour plot; (**b**) velocity contour plot.

Figure 6 shows that the inertia of the satellite droplet is significantly larger than that of the main droplet. As shown in Figure 6b, the satellite droplet merges with the main droplet because the flying speed of the former is significantly greater than that of the latter during the t = 18–22 μs period. However, the satellite droplet slows down to the same speed as the main droplet from t = 22 μs to t = 24 μs and is slower than the main droplet from t = 24 μs to t = 30 μs. Therefore, the satellite droplet cannot merge with the main droplet.

As shown in Figure 7, after detaching from the nozzle and flying towards the substrate, the main droplet came in contact with the substrate (sand particles) at t = 82 μs and was deposited onto the substrate (infiltrate the substrate). The droplet surface was perpendicular to the substrate initially and then swelled as it infiltrated the substrate (t = 84–86 μs). The droplet shrank towards the end of the infiltration process (t = 86–88 μs) and fully infiltrated the substrate at t = 90 μs.

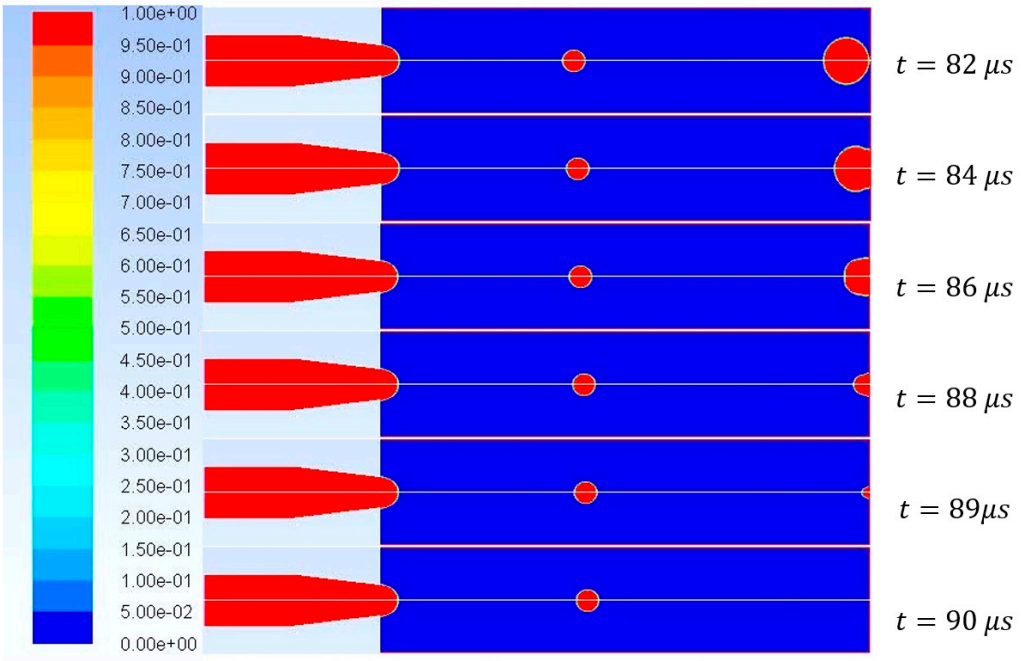

Figure 7. Droplet deposition process.

6.2. Effects of Velocity Amplitude (v_{max}) on Jetting Quality

The vibrational velocity of the piezoelectric actuator is a primary factor determining whether a regular or a spherical droplet will be formed. It also determines the maximum jetting frequency of the printhead. Figure 8 illustrates the effects of vibrational velocity on microdroplet formation and jetting. Table 2 summarizes the results obtained with each value of v_{max}.

Figure 8 shows that a microdroplet will not be formed if the vibrational velocity of the piezoelectric actuator is too low. At v_{max} = 1.8 m/s, the droplet could not detach from the nozzle as the change in volume in the working chamber was too small. If the composite diaphragm deforms by the optimum amount, a droplet will be formed without a satellite droplet, which is indicative of good jetting quality (e.g., v_{max} = 2.0 m/s and 2.2 m/s; Figure 8b). However, if the deformation of the composite diaphragm is too large, a satellite droplet will be formed with the main droplet (i.e., v_{max} = 2.5 m/s). Furthermore, the satellite droplet will not merge with the main droplet. The presence of satellite droplets during actual production processes affect the dimensional accuracy and quality of the final product adversely. Figure 9 demonstrates the relationship between the single-nozzle flow rate and velocity amplitude.

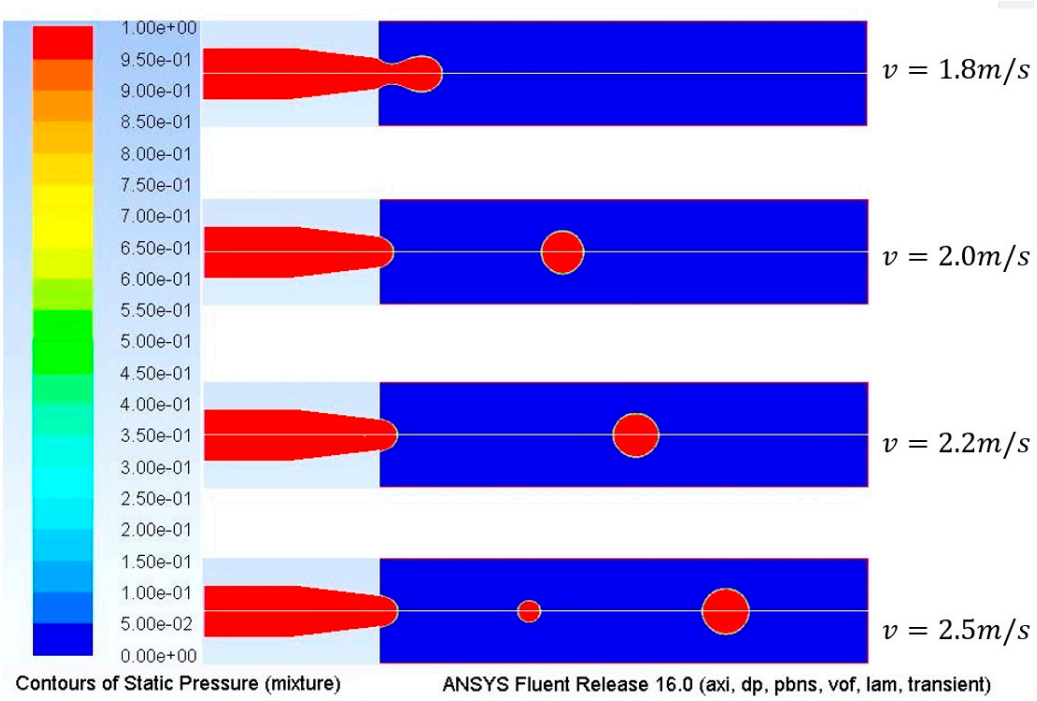

(**a**)

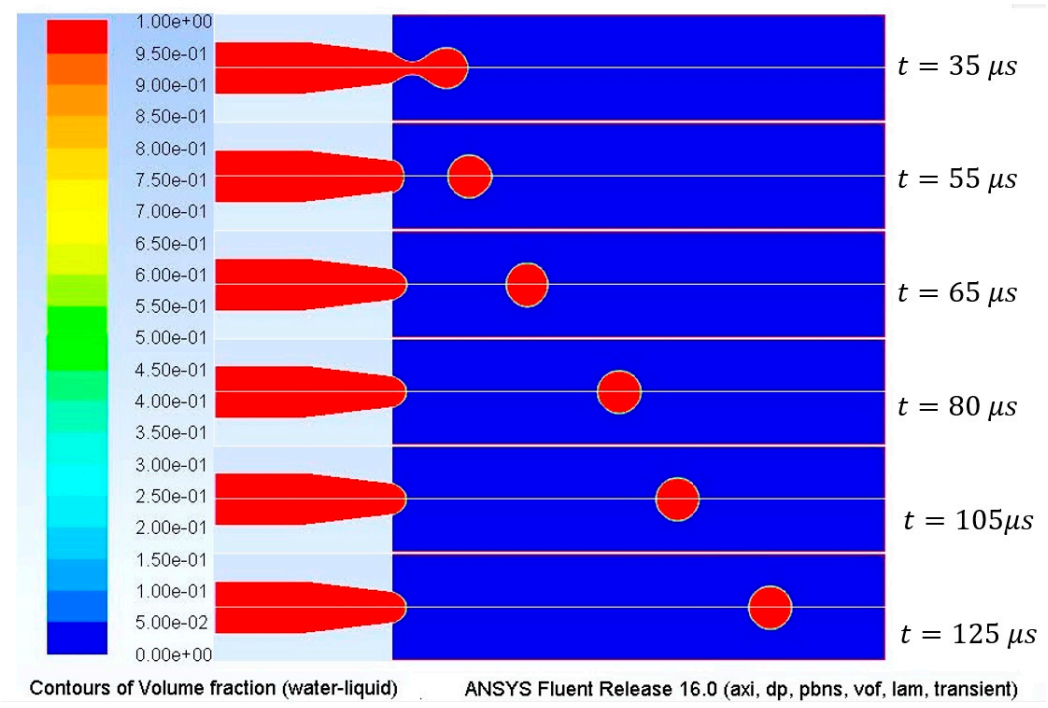

(**b**)

Figure 8. Changes in droplet jetting with different v_{max} values, (**a**) droplet states at t = 60 µs with different v_{max}; (**b**) jetting process at v_{max} = 2.000 m/s.

In this simulation, the nozzle radius was varied to investigate how it affects droplet formation and jetting (Figure 10). At r = 0.006 mm and 0.010 mm, satellite droplets that could not merge with the main droplet were formed. Furthermore, at r = 0.006 mm, a long "tail" was formed instead of a regularly shaped droplet. At r = 0.010 mm, the droplet

separated to form many small satellite droplets. Although a satellite droplet was formed at r = 0.007 mm and 0.008 mm, the satellite droplet was able to catch up to the main droplet and merge to form a new droplet (the relationship between single-nozzle flow rate and nozzle radius is shown in Figure 11). Therefore, prior to the actual production process, the minimum standoff distance should be made larger than the merging distance of the satellite droplets.

Table 2. Droplet formation and jetting at different vmax.

Velocity Amplitude m/s	Droplet Was Formed	Satellite Droplet Was Formed	Satellite Droplet Merged with the Main Droplet	Satellite Droplet at t = 60 μs	Single-Nozzle Flow Rate 10^{-16} kg/s
1.800	No	—	—	—	1.0636
2.000	Yes	No	—	—	3.1662
2.200	Yes	No	—	—	7.3410
2.500	Yes	Yes	No	Yes	12.0763

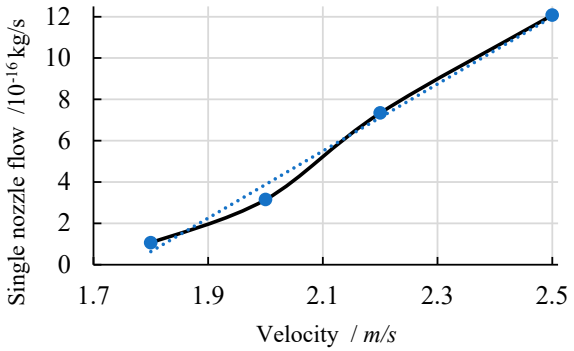

Figure 9. Relationship between velocity amplitude and single-nozzle flow rate.

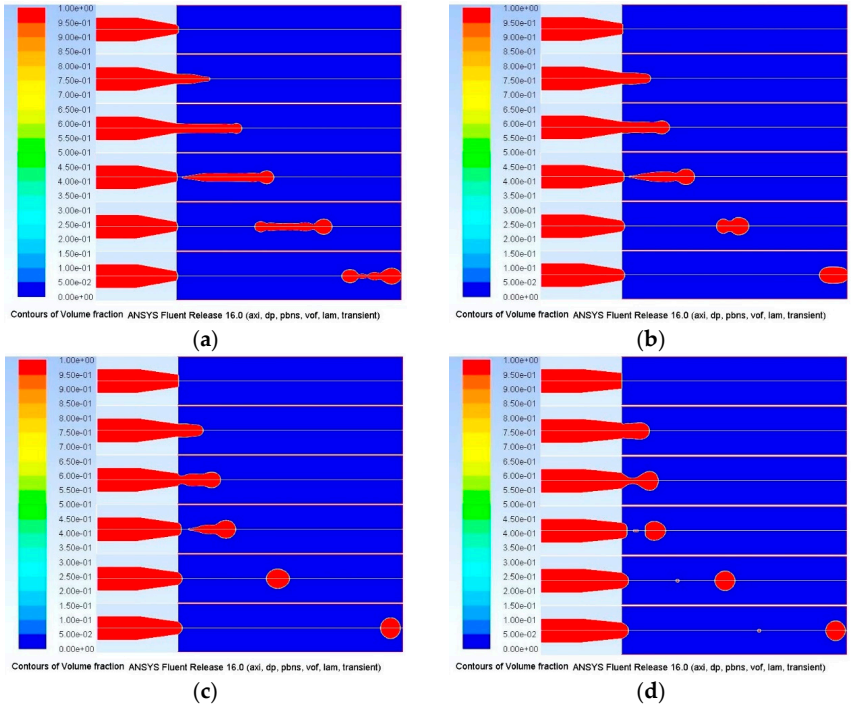

Figure 10. Droplet jetting states with different nozzle radii, (**a**) r = 0.006 mm; (**b**) r = 0.007 mm; (**c**) r = 0.008 mm; (**d**) r = 0.010 mm.

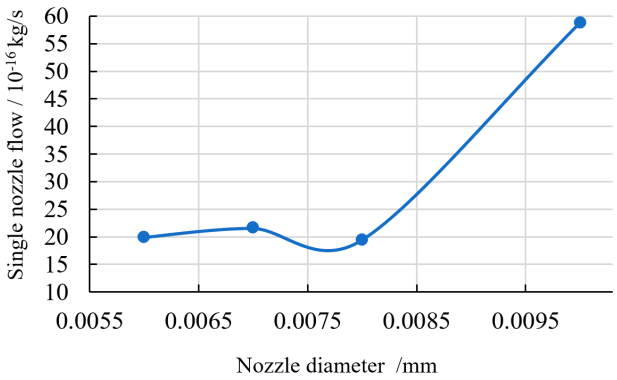

Figure 11. Relationship between nozzle radius and single-nozzle flow rate.

6.3. Effects of Fluid Viscosity on the Jetting Process

Furan resin was used as the jetted fluid in this experiment, and laminar flow was selected as the flow type. However, the simulations (as shown in Figure 12) demonstrate that turbulence can be produced while maintaining all other parameters at a constant level by altering fluid viscosity.

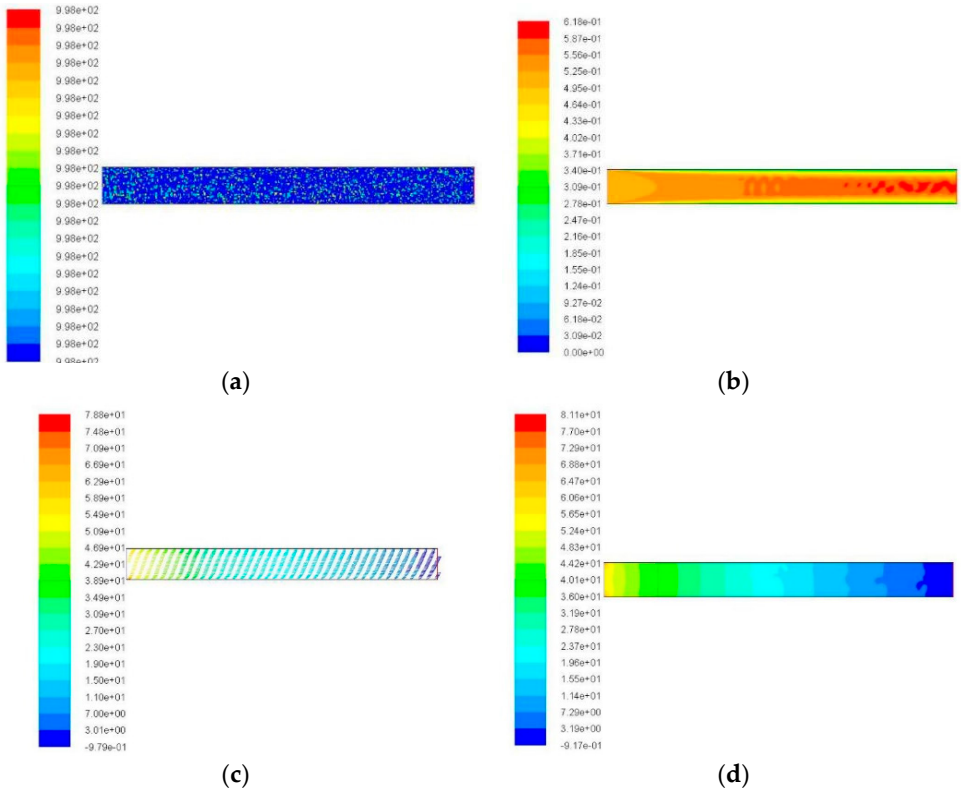

Figure 12. Turbulence analysis, (**a**) turbulence intensity; (**b**) turbulence velocity distribution; (**c**) pressure vector plot; (**d**) pressure plot.

The turbulent flow's pressure distribution was wave-like, as seen above, and the channel's ends had erratic flows. Therefore, the fluid's turbulent fluxes were examined using transient observation and unsteady analysis.

Turbulence was generated by the fluid flow mechanism, which included fluid interactions (such as fluid–wall and intermolecular interactions) inside the chamber and anisotropic drag in the air domain. Figure 13 depicts the droplet jetting condition corresponding to each fluid viscosity.

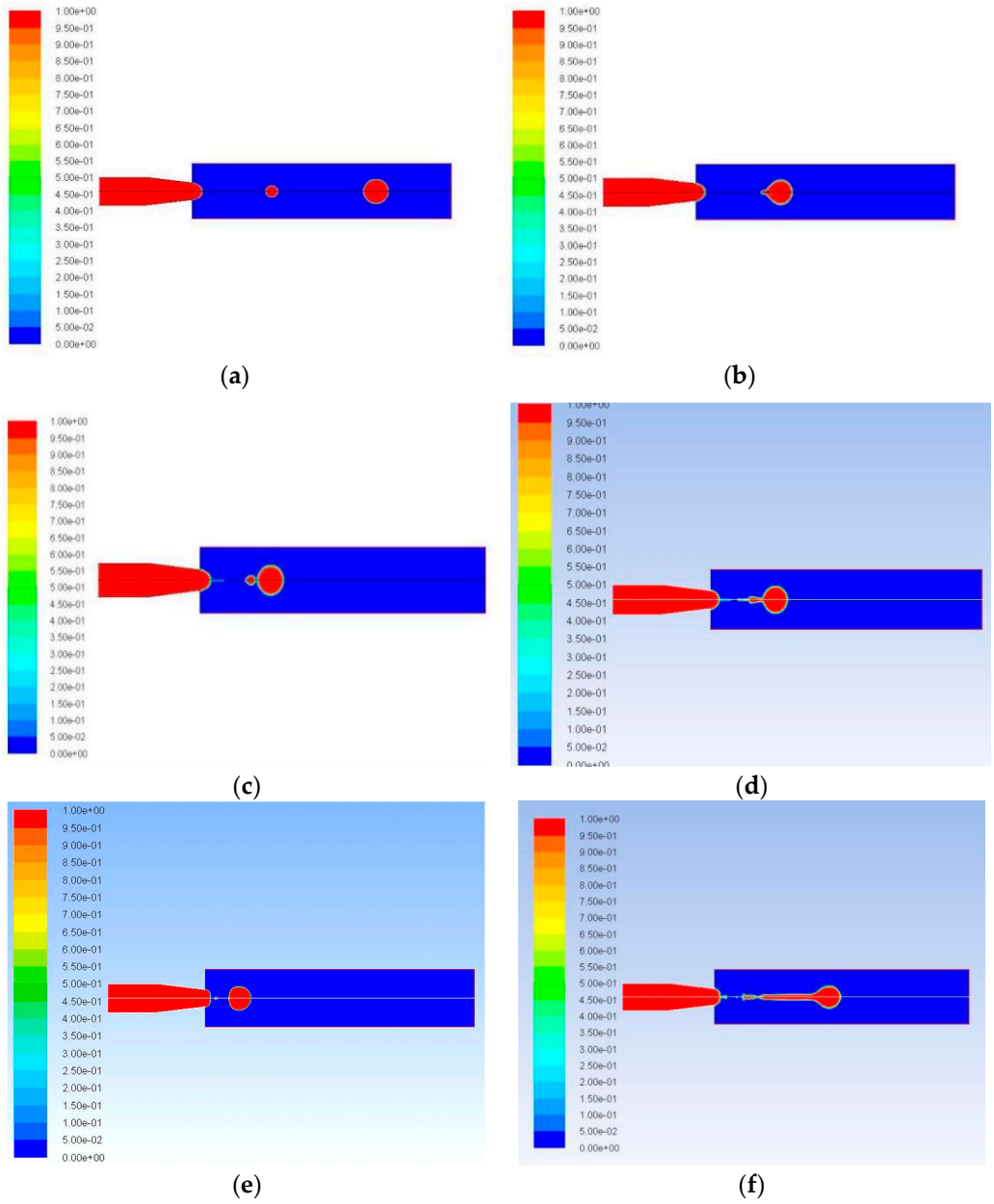

Figure 13. Droplet jetting state at each level of fluid viscosity, (**a**) 1.00 cp; (**b**) 1.80 cp; (**c**) 2.71 cp; (**d**) 4.28 cp; (**e**) 7.25 cp; (**f**) 9.00 cp.

The results of the simulation show that fluid viscosity affects jetting quality and the flight of the satellite droplets. At very low viscosities, satellite droplets that cannot merge with the main droplet are generated during the jetting process. Increasing the viscosity by a reasonable amount, e.g., up to 2.71 cp or 4.28 cp, allows the satellite droplet to catch up with the main droplet; the "catch-up time" was shorter at 2.71 cp than at 4.28 cp. Energy losses during the jetting process are greater at higher viscosities than at lower viscosities, leading to longer catch-up times. At excessively high viscosities (9.00 cp), the jetted droplets exhibit a long "tail," which indicates that the droplet formation process (which includes column stretching, neck shrinking, droplet breaking, and stable movement) stopped at the jetting stage.

7. Discussion

Based on the aforementioned simulation results, it can be deduced that the droplet deposition diffusion rate, which is influenced by process variables such as nozzle aperture, pulse width, inlet velocity, and liquid viscosity, directly affects the mechanical properties and dimensional accuracy of the printed sand model.

Stretching, neck contraction, column breakdown to produce microdroplets, and steady motion are the typical steps in the droplet production process, which is controlled by the physical properties of the printer nozzle. As these stages change, satellite droplets are created. The paper's quality might be impacted by satellite droplets. Therefore, it is possible to combine satellite droplets by slowing down or speeding up their drop rate.

The minimum separation distance must be greater than the satellite droplet convergence distance, per the simulation of droplet flight. According to the findings of the effects of nozzle radius on droplet generation and injection, changing the nozzle's radius will affect the time when the satellite droplet contacts the main droplet. The satellite droplet gradually disappears when the nozzle's radius is decreased. However, a particular drop distance is required for the interaction of satellite and primary droplets. The modeling results indicate that satellite and main droplets can merge when the injection distance exceeds 1.24 mm. Consequently, a minimum printing distance of 1.24 mm must be maintained between the printing head nozzle and the substrate during actual manufacturing.

Additionally, the viscosity of the jet fluid is the most influential factor on jet performance. The fluid's viscosity must fall within the acceptable range of the printer. The lower the fluid's viscosity, the more challenging it is to achieve consistent injection control. Under the condition of suitably increasing viscosity, droplets formed under identical conditions become more uniform.

The result processing graph demonstrates that the driving voltage during the simulation experimental investigation is positively correlated with the droplet velocity, and the voltage is also positively correlated with the microdrop volume; therefore, the driving voltage can be considered to be positively correlated with the microdrop mass. Therefore, the simulation is consistent with the study law of the conversion velocity.

As a reference for the optimization and design of droplet injection technology, the purpose of this study is to propose a more direct and efficient method for optimizing the droplet injection parameters. However, this research does have certain limitations. In this paper, just four influence parameters are selected for optimization and sensitivity analysis. Other determining parameters, such as driving signal amplitude and nozzle structure size, require additional study. The findings of the sensitivity analysis of the influencing factors show that the ink density has the greatest impact, but it appears that this result requires additional verification and analysis based on the entire impact mechanism. Future research will investigate these limits in greater depth.

8. Conclusions

In this study, the jet characteristics of a piezoelectric printhead and the factors affecting print quality were investigated using a combination of theoretical analysis and finite element simulations. These factors include the internal structure of the piezoelectric printhead, actuation parameters, and physical characteristics of the fluid.

To simulate the fluid domain and microdroplet movements in the air domain, a two-phase volume-of-fluid model was developed. Consequently, a qualitative investigation of the jetting processes of a single microdroplet, including its column extending, neck shrinking, breaking, steady movement, and deposition stages, was conducted.

At each of the aforementioned steps, the condition of the droplet is significantly affected by the process parameters. For example, the pulse width of the piezoelectric actuation signal has a positive association with droplet volume and can be changed to enhance droplet volume distribution and eliminate satellite droplets. The actuation voltage controls the vibrational amplitude of the composite diaphragm, which can be lowered to restrict droplet volume and prevent the generation of satellite droplets. However, a very

low actuation voltage may impede microdroplet production, as the droplet's capacity to split from the fluid may not be supported by the volume change adequately. When given a fixed set of settings, increasing the viscosity of the jetting fluid reduces and eliminates the size of the satellite droplet. Nozzle radius is another critical factor determining the formation of satellite droplets and the occurrence of "continuous jetting."

This research will aid in the development of control systems that will boost the precision of inkjet printing for sand mold casting.

Author Contributions: Conceptualization, H.L. and F.P.; methodology, T.L.; software, H.L.; validation, T.L.; formal analysis, F.P. and X.N.; investigation, H.L. and T.L.; resources, H.L.; data curation, H.L.; writing—original draft preparation, H.L.; writing—review and editing, T.L. and X.N.; project administration, H.L.; funding acquisition, H.L. All authors have read and agreed to the published version of the manuscript.

Funding: This research was funded by the National Natural Science Foundation of China [51965001 0708, 2019]; and the Natural Science Foundation of Ningxia [2021AAC03196].

Institutional Review Board Statement: Not applicable.

Informed Consent Statement: Not applicable.

Data Availability Statement: Not applicable.

Acknowledgments: The authors would like to thank Kocel Machinery Limited for experimental equipment and application verification support for the conclusions of this study.

Conflicts of Interest: The authors declare no conflict of interest.

References

1. Ahmed, W.F.; Sghaier, M.B.H.; Allaoui, S. Investigation of the effect of three-point bending testing parameters on the behavior of 3D printed sand. *Int. J. Adv. Manuf. Technol.* **2022**, *121*, 1415–1428. [CrossRef]
2. Chun, S.Y.; Kim, T.; Ye, B.; Lee, M.J.; Lee, G.; Jeong, B.; Lee, H.; Kim, H.D. Penetrated surface characteristics of cement—Mixed sand in powder bed 3D printing. *J. Asian Ceram. Soc.* **2022**, *10*, 306–313. [CrossRef]
3. Dana, H.R.; El Mansori, M. Mechanical characterisation of anisotropic silica sand/furan resin compound induced by binder jet 3D additive manufacturing technology. Ceramics International. *Ceram. Int.* **2020**, *46*, 17867–17880. [CrossRef]
4. Hackney, P.M.; Wooldridge, R. Characterisation of direct 3D sand printing process for the production of sand cast mould tools. *Rapid Prototyp. J.* **2017**, *23*, 7–15. [CrossRef]
5. Liu, Y.; Wang, J. Research on Integration and Control Methods of 3D Array Printhead. *MW Met. Form.* **2016**, *15*, 8–10.
6. Coniglio, N.; Sivarupan, T.; El Mansori, M. Investigation of process parameter effect on anisotropic properties of 3D printed sand molds. *Int. J. Adv. Manuf. Technol.* **2018**, *94*, 2175–2185. [CrossRef]
7. Feng, Y.; Liu, J.; Li, K.; Li, H.; Deng, J.; Liu, Y. Waveform Optimization of Piezoelectric Micro-Jet for the Control of Metal Micro-Droplet Ejection. *Ieee Trans. Ind. Electron.* **2022**, *69*, 3967–3976. [CrossRef]
8. Goto, I.; Kurosawa, K.; Matsuki, T. Effect of 3D-printed sand molds on the soundness of pure copper castings in the vicinity of as-cast surfaces. *J. Manuf. Process.* **2022**, *77*, 329–338. [CrossRef]
9. Hernandez, F.; Fragoso, A. Fabrication of a Stainless-Steel Pump Impeller by Integrated 3D Sand Printing and Casting: Mechanical Characterization and Performance Study in a Chemical Plant. *Appl. Sci.* **2022**, *12*, 3539. [CrossRef]
10. Kang, J.-w.; Ma, Q.-x. The role and impact of 3D printing technologies in casting. *China Foundry* **2017**, *14*, 157–168. [CrossRef]
11. Le Neel, T.A.; Mognol, P.; Hascoet, J.-Y. A review on additive manufacturing of sand molds by binder jetting and selective laser sintering. *Rapid Prototyp. J.* **2018**, *24*, 1325–1336. [CrossRef]
12. Lei, T.; Liu, H.; Ma, C.; Han, J. Optimal Design of Droplet Ejection for PZT Printhead Based on Surrogate Model. *Appl. Sci.* **2022**, *12*, 11683. [CrossRef]
13. Liu, H.; Gao, Y.; Ding, S.; Peng, F.; Zhu, D. Research on the effect of the waveform on the droplet injection behavior of a piezoelectric printhead and the forming accuracy of casting sand molds. *Int. J. Adv. Manuf. Technol.* **2019**, *100*, 251–261. [CrossRef]
14. Liu, H.; Lei, T.; Ma, C.; Peng, F. Optimization of driven waveform of piezoelectric printhead for 3D sand-printing. *Addit. Manuf.* **2021**, *37*, 101627. [CrossRef]
15. Miyanaji, H.; Momenzadeh, N.; Yang, L. Effect of printing speed on quality of printed parts in Binder Jetting Process. *Addit. Manuf.* **2018**, *20*, 1–10. [CrossRef]
16. Oktavianty, O.; Kyotani, T.; Haruyama, S.; Kaminishi, K. New actuation waveform design of DoD inkjet printer for single and multi-drop ejection method. *Addit. Manuf.* **2019**, *25*, 522–531. [CrossRef]
17. Sama, S.R.; Wang, J.; Manogharan, G. Non-conventional mold design for metal casting using 3D sand-printing. *J. Manuf. Process.* **2018**, *34*, 765–775. [CrossRef]

18. Shahmirzadi, M.R.; Gholampour, A.; Kashani, A.; Ngo, T.D. Shrinkage behavior of cementitious 3D printing materials: Effect of temperature and relative humidity. *Cem. Concr. Compos.* **2021**, *124*, 104238. [CrossRef]
19. Sivarupan, T.; Balasubramani, N.; Saxena, P.; Nagarajan, D.; El Mansori, M.; Salonitis, K.; Jolly, M.; Dargusch, M.S. A review on the progress and challenges of binder jet 3D printing of sand moulds for advanced casting. *Addit. Manuf.* **2021**, *40*, 101889. [CrossRef]
20. Sivarupan, T.; El Mansori, M.; Coniglio, N.; Dargusch, M. Effect of process parameters on flexure strength and gas permeability of 3D printed sand molds. *J. Manuf. Process.* **2020**, *54*, 420–437. [CrossRef]
21. Wang, J.; Sama, S.R.; Manogharan, G. Re-Thinking Design Methodology for Castings: 3D Sand-Printing and Topology Optimization. *Int. J. Met.* **2019**, *13*, 2–17. [CrossRef]
22. Zhao, D.; Guo, W.; Zhang, B.; Gao, F. 3D sand mould printing: A review and a new approach. *Rapid Prototyp. J.* **2018**, *24*, 285–300. [CrossRef]
23. Zhao, D.; Guo, W.; Zhang, B.; Gao, F. Research on key technique of line forming for 3D sand mould printing based on quantitative analysis of binder content. *Rapid Prototyp. J.* **2019**, *25*, 62–75. [CrossRef]
24. Wei, D.; Zhang, R.; Wu, R.; Haoying, Z. Design of piezoelectric micro-droplet injector. *J. Tsinghua Univ. (Sci. Technol.)* **2004**, *44*, 1107–1110.
25. Zhao, D.; Zhou, H.; Wang, Y.; Yin, J.; Huang, Y. Drop-on-demand (DOD) inkjet dynamics of printing viscoelastic conductive ink. *Addit. Manuf.* **2021**, *48*, 102451. [CrossRef]